Detection and Visual Analysis of Pathological Abnormalities in Diffusion Tensor Imaging with an Anomaly Lens

M. Bareth[1†], S. Groeschel[2], J. Gruen[1], P. Pretzel[2], T. Schultz[1,3]

[1]University of Bonn, Germany [2]University Children's Hospital Tuebingen, Germany [3]Lamarr Institute for Machine Learning and Artificial Intelligence

Abstract

In clinical practice, Diffusion Tensor Magnetic Resonance Imaging (DT-MRI) is usually evaluated by visual inspection of grayscale maps of Fractional Anisotropy or mean diffusivity. However, the fact that those maps only contain part of the information that is captured in DT-MRI implies a risk of missing signs of disease. In this work, we propose a visualization system that supports a more comprehensive analysis with an anomaly score that accounts for the full diffusion tensor information. It is computed by comparing the DT-MRI scan of a given patient to a control group of healthy subjects, after spatial coregistration. Moreover, our system introduces an Anomaly Lens which visualizes how a user-specified region of interest deviates from the controls, indicating which aspects of the tensor (norm, anisotropy, mode, rotation) differ most, whether they are elevated or reduced, and whether their covariation matches the covariances within the control group. Applying our system to patients with metachromatic leukodystrophy clearly indicates regions affected by the disease, and permits their detailed analysis.

CCS Concepts

• ***Visualization application domains*** → *Visual analytics;* • ***Life and medical sciences*** → *Health informatics;*

1. Introduction

Traditionally, medical images are evaluated by visual inspection: A trained radiologist compares the images to their mental model of healthy anatomy. However, without additional support, subtle signs of disease can escape visual detection. Therefore, visualization systems have been proposed that use spatial coregistration to detect and highlight differences from a normal cohort [HGF*05,MBF15], or in longitudinal data from the same subject [SBR*22].

Diffusion Tensor Magnetic Resonance Imaging (DT-MRI) [PJB*96] is widely used to characterize microstructural changes in the brain. However, it is particularly challenging to evaluate, since it yields a 3×3 symmetric matrix in each voxel, the diffusion tensor. For visual inspection, the diffusion tensor is often reduced to scalars such as mean diffusivity (MD) or Fractional Anisotropy (FA), which however only contain part of its information [PB96]. Tensor glyphs [KW06] visually encode the full tensor information, but are more suitable for a detailed investigation at specific locations than to obtain an overview of a full DT-MRI volume [SV19].

Our work presents the first visualization system for comparing a DT-MRI scan from a given patient to a healthy control group, based on a voxel-wise anomaly score that accounts for the full DT-MRI information. Our system supports rapid navigation to slices with strong overall deviations from the control group, and an in-depth investigation of those differences with a novel visual encoding, the Anomaly Lens (Section 4). It is based on a novel decomposition of the overall anomaly score into a sum of interpretable terms, which we describe in Section 3. In Section 6, we demonstrate how our system can be used to detect and analyze abnormalities in patients with metachromatic leukodystrophy [MHS*21].

2. Related Work

While visualization techniques have been proposed for comparing pairs of tensor fields [ZSL*16], or groups (ensembles) of tensor fields [ZHC*17, AWSW*19], to the best of our knowledge, our current system is the first to visualize anomalies by comparing an individual tensor field to an ensemble that serves as a reference.

Outside medical imaging, the integration of automated anomaly detection into interactive systems for visual exploration and interpretation has a long history. Such systems have been proposed for intrusion detection in computer networks [TMWJK04], for spatiotemporal data, as it arises in maritime [RFZ08] or traffic surveillance [CLZ*18], as well as in social media [CTB*12], and in event sequences, which might reflect medical treatments in electronic health records, or career paths in academia [GJC*22].

A key part of our visualization system is the Anomaly Lens, an interactive lens [BSP*93, TGK*16] that displays more detailed information about anomalies in a user-selected brain region. Even

† M. Bareth performed this work at the University of Bonn, but is now with the Alfred Wegener Institute in Bremerhaven, Germany

DOI: 10.2312/evs.20231041

though the visual analytics system EnsembleLens [XXM*19] also addresses anomaly detection, it has an entirely different focus than our work, comparing results from multiple anomaly detection algorithms, and it uses the term "lens" in a more abstract way, since it has been designed for data without an intrinsic spatial structure.

3. Theory

In our context, anomaly detection is the task of finding locations in which the DT-MRI volume of a given patient differs significantly from a set of DT-MRI volumes that have been taken from a matching healthy control group. To enable a voxel-wise comparison, we first bring all datasets into spatial alignment using a specialized nonlinear registration algorithm that accounts for the required reorientation of diffusion tensors [ZAY*07].

As an anomaly score, we use the well-established Mahalanobis distance [Mah36] between a multivariate distribution with mean μ and covariance matrix Σ, and a point $\mathbf{x}$. It is defined as

$$d_M = \sqrt{(\mathbf{x}-\mu)^T \Sigma^{-1} (\mathbf{x}-\mu)}. \tag{1}$$

We compute d_M voxel-wise by first embedding the diffusion tensors $\mathbf{T}$ isometrically into $\mathbb{R}^6$ via

$$\mathbf{t} = [T_{11}, T_{22}, T_{33}, \sqrt{2}T_{12}, \sqrt{2}T_{13}, \sqrt{2}T_{23}]^T, \tag{2}$$

which yields the representation $\mathbf{x}$ of the patient's diffusion tensor, and permits computation of voxel-wise sample means $\mu \in \mathbb{R}^6$ and covariances $\Sigma \in \mathbb{R}^{6\times 6}_{\text{Sym}}$ from the control group.

A high value of d_M indicates dissimilarity from the healthy cohort. To interpret it, we would like to know *how* the patient differs: Does a decrease of anisotropy, possibly going along with an increase in overall diffusivity, suggest a loss of structural tissue organization? Does it go along with changes between planar and more linear anisotropy in a region of crossing fibers?

To permit such an investigation, we express the difference $\mathbf{x}-\mu$ between the patient's diffusion tensor and the control group mean in a specific orthonormal basis, using a matrix $\mathbf{Q}$. The coefficients of the difference vector in that basis are given as

$$\delta = \mathbf{Q}(\mathbf{x}-\mu) = [\delta_{\text{norm}}, \delta_{\text{FA}}, \delta_{\text{mode}}, \delta_{r_1}, \delta_{r_2}, \delta_{r_3}]^T \tag{3}$$

and can be interpreted as differences that relate to changes in Frobenius norm (i.e., overall amount of diffusivity), Fractional Anisotropy (FA), tensor mode (i.e., difference between linear and planar anisotropy), and rotations around the three eigenvectors. $\mathbf{Q}$ needs to be computed per-voxel, depending on the local value of μ. Since it is derived from the gradients of tensor invariants and the tangents of infinitesimal rotations, it is referred to as the IGRT ("invariant gradient and rotation tangent") basis [KEWW07].

While the IGRT basis has been used previously for tensor field visualization [AWHS16, AWSW*19], our current work is the first to use it in the context of anomaly detection. In particular, we use it to derive a novel decomposition of the squared Mahalanobis distance into a sum of interpretable terms. We first observe that, due to orthogonality of $\mathbf{Q}$, evaluating the Mahalanobis distance in the IGRT basis with a suitably transformed covariance, $\mathbf{S} = \mathbf{Q}\Sigma\mathbf{Q}^T$, yields the same result as Equation (1),

$$d_M = \sqrt{\delta^T \mathbf{S}^{-1} \delta} = \sqrt{\sum_{i=1}^{6}\sum_{j=1}^{6} \mathbf{S}^{-1}_{ij} \delta_i \delta_j}, \tag{4}$$

where the coefficients of δ, whose names in Equation (3) reflected their meaning, have now been numbered to simplify notation.

Next, we observe that, due to the use of the IGRT basis, the 36 terms in the double sum in Equation (4) can be interpreted as follows: The 6 diagonal terms $(i = j)$ involve squared coefficients of δ, normalized by the corresponding diagonal element of the precision matrix $\mathbf{S}^{-1}$. They attain high values if the deviation between the patient's diffusion tensor and the mean of the control group with respect to norm, FA, mode, and the three rotations is large, relative to the corresponding variability within the control group.

Due to symmetry, 15 of the 30 remaining terms are unique. They involve products of two different coefficients of δ, multiplied by an off-diagonal element of $\mathbf{S}^{-1}$. These terms decrease or increase the value of d_M depending on whether the covariation between different aspects of the patient's diffusion tensor matches the covariances in the control group. For example, if norm and FA were negatively correlated in the control group, a given absolute deviation in norm and FA from the group mean will be considered less anomalous if it matches this in that both measures deviate in opposite directions.

This interpretation is based on the relationship between the off-diagonal elements of $\mathbf{S}^{-1}$ and partial correlations in the control group. The partial correlation between δ_i and δ_j (controlling for the set R of all remaining indices) can be computed as

$$\rho_{ij.R} = -\frac{\mathbf{S}^{-1}_{ij}}{\sqrt{\mathbf{S}^{-1}_{ii}\mathbf{S}^{-1}_{jj}}}. \tag{5}$$

Therefore, the negative partial correlation between norm and FA in our example would amount to a positive sign of $\mathbf{S}^{-1}_{\text{norm, FA}}$. If a patient has increased tensor norm, but decreased FA, the resulting product $\mathbf{S}^{-1}_{\text{norm, FA}}\,\delta_{\text{norm}}\,\delta_{\text{FA}}$ will be negative.

We reduce the resulting 21 unique terms to a more manageable number of 10 for visual encoding. This is achieved by combining the rotational degrees of freedom, which would be difficult to interpret individually. Therefore, we treat the partial sum that involves the three diagonal terms related to rotation, and the corresponding three unique off-diagonal terms, as a single value. Moreover, partial sums of off-diagonal terms that relate each of the three shape dimensions to the three rotational degrees of freedom are treated as one value each for norm, FA, and mode.

Since we decomposed the *squared* Mahalanobis distance, we visualize the square roots of the resulting absolute values, preserving their signs. This leaves the following 10 values for visual encoding:

- **V1** 3 non-negative values indicating deviations with respect to tensor shape, i.e., norm, FA, and mode
- **V2** 1 non-negative value indicating overall deviations with respect to rotation
- **V3** 3 signed values indicating to which extent the covariation between tensor shape coefficients matches the control group
- **V4** 3 signed values indicating to which extent the covariance between tensor shape and rotation matches the control group

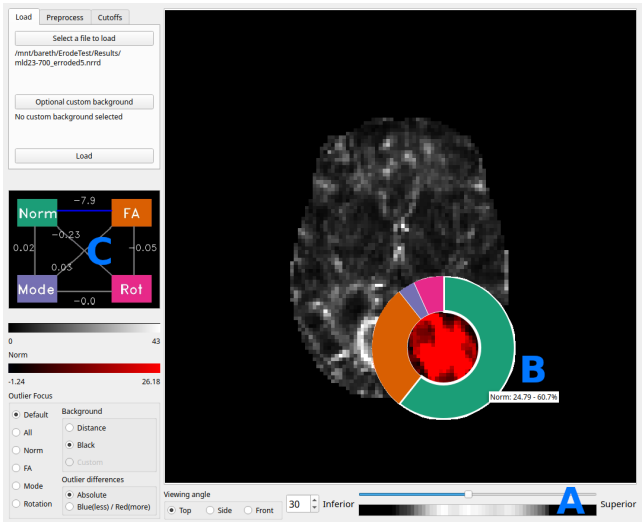

Figure 1: *Key features of our visualization system are (A) a mechanism for fast navigation to slices in which a patient differs most strongly from the control group, (B) an Anomaly Lens that conveys which aspects of the diffusion tensor differ most, and in which direction, and (C) a Covariance View that indicates whether the covariation of different aspects within the Anomaly Lens matches the expectation from the control group.*

4. Visual Encoding and Interaction

Traditional evaluation of DT-MRI involves visual inspection of MD and FA maps, as they are shown in Figure 3 B and C, without specific guidance. It would not detect abnormalities that do not affect MD or FA. Our visualization aims to make this process faster and more comprehensive by supporting three tasks: First, guiding the viewer towards regions of strongest deviations from the control group. Second, finding out which aspects of the diffusion tensor, such as norm or anisotropy, differ most within a given region, and whether they are elevated or reduced. Third, finding out to which extent the relative directions in which different aspects of the tensor deviate from the group mean agree with the covariation that was observed within that region in the control group.

Figure 1 shows an overview of our system. For the initial task of guiding the user towards anomalous regions, we visualize the Mahalanobis distance d_M by color coding it on slice views. To avoid confusion with color schemes that are used later on, we use a basic grayscale mapping at this point, so that high values stand out as bright. To permit rapid navigation to slices that contain strong overall anomalies, we additionally visualize the cumulative value of d_M for each slice below the slider that is to browse slices (Figure 1 A).

The Anomaly Lens (Figure 1 B) supports the second task, a more detailed analysis of local anomalies. It covers a user-defined circular region of interest, and is placed by clicking on its desired center and releasing the mouse button after moving to the desired radius. The Anomaly Lens is shown as a ring that is subdivided into four differently colored segments. Their relative sizes match the relative magnitudes of the four values from **V1** and **V2**, averaged over the interior of the lens. Thus, they indicate the relative contributions of norm (green), FA (orange), mode (purple), and rotation (pink) to the overall anomaly scores within the lens region. Labels and exact absolute and relative values can be shown as tooltips. For example, the ring in Figure 1 indicates that the local anomaly is mostly due to deviations in norm, followed by deviations in FA, while mode and rotation had relatively little contribution.

Double clicking on one of the segments highlights it with a white boundary, and reveals whether the corresponding attributes were above or below the reference from the control group by color coding the respective voxel-wise values in the interior of the lens. Even though the values in **V1** and **V2** are non-negative, we use a diverging color map, with blue indicating locally reduced values, red elevated ones, based on the sign of the corresponding coefficient δ_i from Equation (3). The red interior of the lens in Figure 1 shows that, within most of this region, norm has been higher than in the controls; the blue interior in Figure 2 shows decreased FA.

A Covariance View supports the third task of analyzing whether the covariation between different aspects of the tensor agree with what was observed in the control group. It is linked to the Anomaly Lens, but is rendered separately (Figure 1 C). It shows the values from **V3** and **V4**, again averaged over the lens region. Since they reflect pairwise relationships, we visualize them as links between nodes that represent norm, FA, mode, and rotation.

Signs are again encoded via a blue (negative) to red (positive) colormap. As discussed in Section 4, they indicate whether or not the relative directions in which the two measures differed from the mean of the control group agree with the corresponding partial correlations in the control group. Positive values, highlighted as red edges, are the surprising findings in which the covariation in the patient differs from the control group. An example is shown in Figure 3. The nodes in the Covariance View are colored so that they serve as a color legend for the ring around the Anomaly Lens.

In Figure 1 C, the strongest edge is a negative one, between norm and FA. Double-clicking on the respective segments of the Anomaly Lens reveals that FA is reduced, while norm is increased. The negative sign of the link between norm and FA in the Covariance View indicates that a corresponding negative partial correlation was observed in the same region in the control group.

5. Implementation

Our system is implemented in Python, using `PyQt` for the graphical user interface. The Anomaly Lens is a custom widget. Diffusion tensors have been estimated with FSL [JBB*12]. We slightly eroded FSL's brain mask to ignore artifacts that often arise close to the outer boundary of the brain. Registration has been performed using the Diffusion Tensor Imaging ToolKit (DTI-TK) [ZAY*07].

The remaining pre-processing (computing voxel-wise means, covariances, and IGRT matrices for the control group, computing the Mahalanobis distance and the values **V1**–**V4**) can be conducted within our tool. All results are stored as files, so that the same data can be analyzed in subsequent sessions without any delay. For a control group of 19 subjects, pre-processing on a standard workstation took almost 8 minutes. The subsequent pre-processing of each patient took 50 seconds.

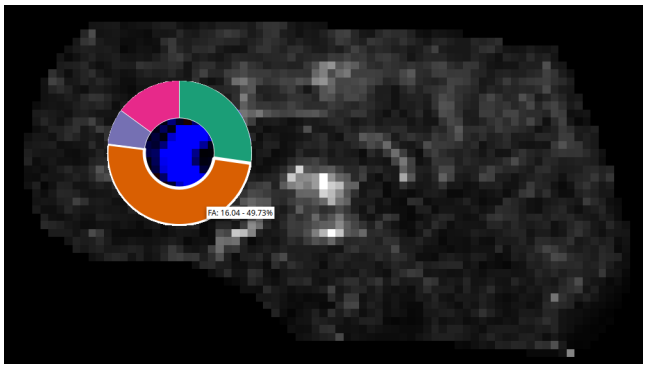

Figure 2: *The anomaly lens indicates that, in the genu of this patient's corpus callosum, a decrease in FA is the strongest single factor of the overall anomaly.*

6. Results

We used our system to analyze abnormalities in DT-MRI data of patients suffering from late-infantile metachromatic leukodystrophy (MLD), a genetic affliction in which an accumulation of sulfatides damages the myelin sheets around neural fibers in the central and peripheral nervous system, leading to progressive motor and cognitive deficiency [SCS*20]. The study was approved by the ethical committee of the University of Tübingen, Germany.

Our DT-MRI data had 30 diffusion-weighted volumes at $b = 700\,\mathrm{s/mm^2}$ and three reference volumes at $b = 0$. Each volume had $96 \times 96 \times 50$ voxels with 2 mm isotropic resolution. We will discuss exemplary findings from three patients, who were compared to an age-matched control group of 19 healthy children.

In the white matter of all three patients, our anomaly scores indicate extensive regions of demyelination, with decreased Fractional Anisotropy (FA) and increased overall diffusivity. An example for the first patient is shown in Figure 1. These changes agree with previously reported findings in another MLD cohort [vRKS*18]. We note that our system uses the Frobenius norm instead of mean diffusivity (MD), which is more widely reported in the clinical literature. This is because our derivation in Section 3 relies on orthogonality of the matrix $\mathbf{Q}$, which would be violated when replacing norm with MD [KEWW07]. Both values quantify overall diffusivity, and they are strongly correlated. In terms of the diffusion tensor eigenvalues, the Frobenius norm is given as $\sqrt{\lambda_1^2+\lambda_2^2+\lambda_3^2}$, while MD is given as $(\lambda_1+\lambda_2+\lambda_3)/3$.

Even though the general pattern of decreased FA and increased overall diffusivity was present in all anomalies, the relative magnitude of those two factors varied. While norm dominated in the previous example, Figure 2 shows an example in which the Anomaly Lens reveals that FA is the strongest single factor in another patient, and a different anatomical region, the genu of the corpus callosum.

Finally, in a coronal slice of the third patient, Figure 3 A shows an example in which the Covariance View (presented as an inset) reveals a remarkable insight: The interaction between FA and mode contributed about as much to the anomaly score as the deviation in mode itself. In this case, FA correlated positively with more linear diffusion tensors in the control group, while the Anomaly Lens shows that the patient had slightly higher-than-average linearity despite decreased FA. This might be explained by one of two crossing fiber bundles being affected more strongly by demyelination. While a radiologist would be able to detect the anomaly in terms of elevated MD (Figure 3 B) and decreased FA (C) by visual inspection, a traditional analysis would not account for changes in mode.

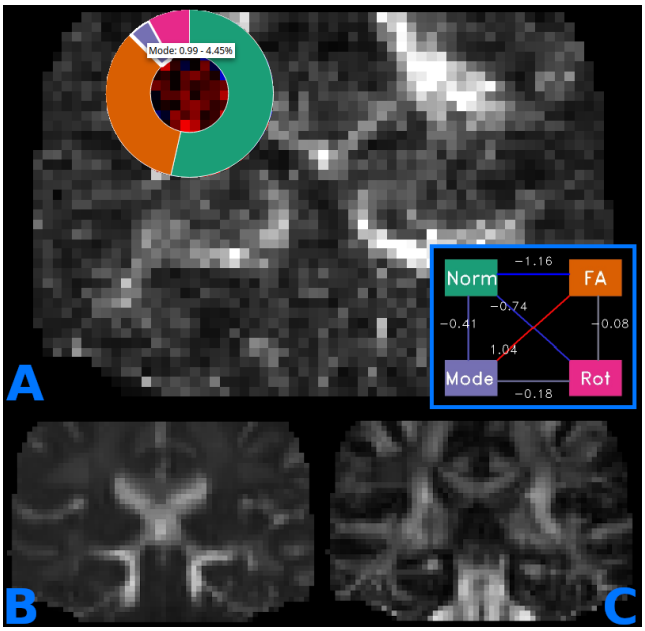

Figure 3: *In this example, the red color for mode in the interior of the anomaly lens (A) indicates a slightly more-linear-than-average tensor shape. Even though this deviation is so subtle that it contributed little to the overall anomaly score, the fact that it co-occured with decreased FA is remarkable, as indicated by the red edge in the Covariance View (inset). This would remain undetected when inspecting maps of MD (B) and FA (C).*

7. Conclusions

We presented an interactive visualization system for the detection and investigation of pathological abnormalities in diffusion tensor imaging. It is based on computing the Mahalanobis distance as an anomaly score that accounts for the multivariate nature of the diffusion tensors, and on decomposing it into individual terms that can be interpreted as being related to tensor norm, FA, mode, rotation, as well as covariations between them. The resulting quantities are encoded in an overview visualization, an Anomaly Lens that reveals the dominant factors in a region of interest, and a Covariance View. In future work, we hope to extend our approach towards even more complex variants of diffusion imaging, such as diffusional kurtosis [JHR*05] or NODDI [ZSWKA12].

Acknowledgments

Funded by the Deutsche Forschungsgemeinschaft (DFG, German Research Foundation) – 422414649.

References

[AWHS16] ABBASLOO A., WIENS V., HERMANN M., SCHULTZ T.: Visualizing tensor normal distributions at multiple levels of detail. *IEEE Trans. on Visualization and Computer Graphics 22*, 1 (2016), 975–984. doi:10.1109/TVCG.2015.2467031. 2

[AWSW*19] ABBASLOO A., WIENS V., SCHMIDT-WILCKE T., SUNDGREN P. C., KLEIN R., SCHULTZ T.: Interactive formation of statistical hypotheses in diffusion tensor imaging. In *EG Workshop on Visual Computing for Biology and Medicine (VCBM)* (2019), pp. 33–43. doi:10.2312/vcbm.20191229. 1, 2

[BSP*93] BIER E. A., STONE M. C., PIER K., BUXTON W., DEROSE T. D.: Toolglass and magic lenses. In *Proc. ACM SIGGRAPH* (1993), pp. 73–80. doi:10.1145/166117.166126. 1

[CLZ*18] CAO N., LIN C., ZHU Q., LIN Y.-R., TENG X., WEN X.: Voila: Visual anomaly detection and monitoring with streaming spatiotemporal data. *IEEE Trans. on Visualization and Computer Graphics 24*, 1 (2018), 23–33. doi:10.1109/tvcg.2017.2744419. 1

[CTB*12] CHAE J., THOM D., BOSCH H., JANG Y., MACIEJEWSKI R., EBERT D. S., ERTL T.: Spatiotemporal social media analytics for abnormal event detection and examination using seasonal-trend decomposition. In *Proc. IEEE Conf. on Visual Analytics Science and Technology (VAST)* (2012), pp. 143–152. doi:10.1109/VAST.2012.6400557. 1

[GJC*22] GUO S., JIN Z., CHEN Q., GOTZ D., ZHA H., CAO N.: Interpretable anomaly detection in event sequences via sequence matching and visual comparison. *IEEE Trans. on Visualization and Computer Graphics 28*, 12 (2022), 4531–4545. doi:10.1109/tvcg.2021.3093585. 1

[HGF*05] HUPPERTZ H.-J., GRIMM C., FAUSER S., KASSUBEK J., MADER I., HOCHMUTH A., SPREER J., SCHULZE-BONHAGE A.: Enhanced visualization of blurred gray–white matter junctions in focal cortical dysplasia by voxel-based 3D MRI analysis. *Epilepsy Research 67*, 1-2 (2005), 35–50. doi:10.1016/j.eplepsyres.2005.07.009. 1

[JBB*12] JENKINSON M., BECKMANN C. F., BEHRENS T. E., WOOLRICH M. W., SMITH S. M.: FSL. *NeuroImage 62*, 2 (2012), 782–790. doi:10.1016/j.neuroimage.2011.09.015. 3

[JHR*05] JENSEN J. H., HELPERN J. A., RAMANI A., LU H., KACZYNSKI K.: Diffusional kurtosis imaging: The quantification of non-gaussian water diffusion by means of magnetic resonance imaging. *Magnetic Resonance in Medicine 53* (2005), 1432–1440. doi:10.1002/mrm.20508. 4

[KEWW07] KINDLMANN G., ENNIS D., WHITAKER R., WESTIN C.-F.: Diffusion tensor analysis with invariant gradients and rotation tangents. *IEEE Trans. on Medical Imaging 26*, 11 (2007), 1483–1499. doi:10.1109/TMI.2007.907277. 2, 4

[KW06] KINDLMANN G., WESTIN C.-F.: Diffusion tensor visualization with glyph packing. *IEEE Trans. on Visualization and Computer Graphics 12*, 5 (2006), 1329–1335. doi:10.1109/tvcg.2006.134. 1

[Mah36] MAHALANOBIS P. C.: On the generalized distance in statistics. *Proc. of the National Institute of Science of India 2*, 1 (1936), 49–55. 2

[MBF15] MARTIN P., BENDER B., FOCKE N. K.: Post-processing of structural MRI for individualized diagnostics. *Quantitative Imaging in Medicine and Surgery 5*, 2 (2015), 188–203. doi:10.3978/j.issn.2223-4292.2015.01.10. 1

[MHS*21] MARTIN P., HAGBERG G. E., SCHULTZ T., HARZER K., KLOSE U., BENDER B., NÄGELE T., SCHEFFLER K., KRÄGELOH-MANN I., GROESCHEL S.: T2-pseudonormalization and microstructural characterization in advanced stages of late-infantile metachromatic leukodystrophy. *Clinical Neuroradiology 31*, 4 (2021), 969–980. doi:10.1007/s00062-020-00975-2. 1

[PB96] PIERPAOLI C., BASSER P. J.: Toward a quantitative assessment of diffusion anisotropy. *Magnetic Resonance in Medicine 36* (1996), 893–906. doi:10.1002/mrm.1910360612. 1

[PJB*96] PIERPAOLI C., JEZZARD P., BASSER P. J., BARNETT A., DI CHIRO G.: Diffusion tensor MR imaging of the human brain. *Radiology 201*, 3 (1996), 637–648. doi:10.1148/radiology.201.3.8939209. 1

[RFZ08] RIVEIRO M., FALKMAN G., ZIEMKE T.: Improving maritime anomaly detection and situation awareness through interactive visualization. In *Proc. Int'l Conf. on Information Fusion* (2008), IEEE, pp. 1–8. 1

[SBR*22] SUGATHAN S., BARTSCH H., RIEMER F., GRÜNER R., LAWONN K., SMIT N.: Longitudinal visualization for exploratory analysis of multiple sclerosis lesions. *Computers & Graphics 107* (2022), 208–219. doi:10.1016/j.cag.2022.07.023. 1

[SCS*20] SHAIMARDANOVA A. A., CHULPANOVA D. S., SOLOVYEVA V. V., MULLAGULOVA A. I., KITAEVA K. V., ALLEGRUCCI C., RIZVANOV A. A.: Metachromatic leukodystrophy: Diagnosis, modeling, and treatment approaches. *Frontiers in Medicine 7* (2020). doi:10.3389/fmed.2020.576221. 4

[SV19] SCHULTZ T., VILANOVA A.: Diffusion MRI visualization. *NMR in Biomedicine 32*, 4 (2019), e3902. doi:10.1002/nbm.3902. 1

[TGK*16] TOMINSKI C., GLADISCH S., KISTER U., DACHSELT R., SCHUMANN H.: Interactive lenses for visualization: An extended survey. *Computer Graphics Forum 36*, 6 (2016), 173–200. doi:10.1111/cgf.12871. 1

[TMWJK04] TEOH S. T., MA K.-L., WU S. F., JANKUN-KELLY T.: Detecting flaws and intruders with visual data analysis. *IEEE Computer Graphics and Applications 24*, 5 (2004), 27–35. doi:10.1109/mcg.2004.26. 1

[vRKS*18] VAN RAPPARD D. F., KÖNIGS M., STEENWEG M. E., BOELENS J. J., OOSTERLAAN J., VAN DER KNAAP M. S., WOLF N. I., POUWELS P. J. W.: Diffusion tensor imaging in metachromatic leukodystrophy. *Journal of Neurology 265*, 3 (2018), 659–668. doi:10.1007/s00415-018-8765-3. 4

[XXM*19] XU K., XIA M., MU X., WANG Y., CAO N.: EnsembleLens: Ensemble-based visual exploration of anomaly detection algorithms with multidimensional data. *IEEE Trans. on Visualization and Computer Graphics 25*, 1 (2019), 109–119. doi:10.1109/tvcg.2018.2864825. 2

[ZAY*07] ZHANG H., AVANTS B. B., YUSHKEVICH P. A., WOO J. H., WANG S., MCCLUSKEY L. F., ELMAN L. B., MELHEM E. R., GEE J. C.: High-dimensional spatial normalization of diffusion tensor images improves the detection of white matter differences: an example study using amyotrophic lateral sclerosis. *IEEE Trans. on Medical Imaging 26*, 11 (2007), 1585–1597. doi:10.1109/TMI.2007.906784. 2, 3

[ZHC*17] ZHANG C., HÖLLT T., CAAN M. W. A., EISEMANN E., VILANOVA A.: Comparative visualization for diffusion tensor imaging group study at multiple levels of detail. In *EG Workshop on Visual Computing for Biology and Medicine (VCBM)* (2017), pp. 53–62. doi:10.2312/vcbm.20171237. 1

[ZSL*16] ZHANG C., SCHULTZ T., LAWONN K., EISEMANN E., VILANOVA A.: Glyph-based comparative visualization for diffusion tensor fields. *IEEE Trans. on Visualization and Computer Graphics 22*, 1 (2016), 797–806. doi:10.1109/TVCG.2015.2467435. 1

[ZSWKA12] ZHANG H., SCHNEIDER T., WHEELER-KINGSHOTT C. A., ALEXANDER D. C.: NODDI: practical in vivo neurite orientation dispersion and density imaging of the human brain. *NeuroImage 61*, 4 (2012), 1000–1016. doi:10.1016/j.neuroimage.2012.03.072. 4